Theor. Comput. Fluid Dyn. (2006) 20(1): 41–54
DOI 10.1007/s00162-005-0001-y

ORIGINAL ARTICLE

I. V. Egorov · A. V. Fedorov · V. G. Soudakov

Direct numerical simulation of disturbances generated by periodic suction-blowing in a hypersonic boundary layer

Received: 25 May 2004 / Accepted: 16 June 2005 / Published online: 19 January 2006
© Springer-Verlag 2005

Abstract A numerical algorithm and code are developed and applied to direct numerical simulation (DNS) of unsteady two-dimensional flow fields relevant to stability of the hypersonic boundary layer. An implicit second-order finite-volume technique is used for solving the compressible Navier–Stokes equations. Numerical simulation of disturbances generated by a periodic suction-blowing on a flat plate is performed at free-stream Mach number 6. For small forcing amplitudes, the second-mode growth rates predicted by DNS agree well with the growth rates resulted from the linear stability theory (LST) including nonparallel effects. This shows that numerical method allows for simulation of unstable processes despite its dissipative features. Calculations at large forcing amplitudes illustrate nonlinear dynamics of the disturbance flow field. DNS predicts a nonlinear saturation of fundamental harmonic and rapid growth of higher harmonics. These results are consistent with the experimental data of Stetson and Kimmel obtained on a sharp cone at the free-stream Mach number 8.

Keywords Hypersonic flow · Boundary layer · Stability · Numerical simulation

1 Introduction

Prediction of laminar-turbulent transition is important for aerothermal design [1, 2] and drag calculations [3] of high-speed vehicles. This motivates extensive experimental, theoretical and numerical studies of transition in supersonic and hypersonic boundary layer flows. Progress made in transition prediction methodology is reviewed by Malik [4]. There are at least two routes to turbulence [5]. The first, which is typical for low disturbance environments, involves: receptivity, linear growth of unstable modes, and nonlinear breakdown to turbulence. The second, which occurs in high-disturbance environments, involves bypass of the linear phase.

For the first route, receptivity and the nonlinear phase are the stumbling blocks of transition prediction. In this case, the state-of-the-art method, for engineering applications, remains the e^N-method [6], which accounts for the linear phase only.

The second route is poorly understood; it is treated empirically [5] using limited wind-tunnel data. Direct numerical simulation (DNS) may help to fill these gaps. Since stability and transition experiments in hypersonic wind tunnels are very limited, reliable numerical experiments seem to be the only way to acquire detailed data on the disturbance-field dynamics related to receptivity, nonlinear breakdown and bypass. Such data can be used for development and verification of theoretical models. They can also be correlated for engineering applications, especially, to highly non-uniform flows, which are not covered by the compressible nonlinear parabolized stability equations (NPSE) [7].

Communicated by M. Y. Hussaini

I. V. Egorov · A. V. Fedorov (✉) · V. G. Soudakov
Moscow Institute of Physics and Technology, 16 Gagarin Street, Zhukovsky, Moscow Region 140180, Russia
E-mail: fedorov@falt.ru

This explains high interest in DNS of different phases of hypersonic transition during the last two decades. Pruett and Chang [8] used combined NPSE and DNS to compute through the transition zone for a Mach 8 boundary layer. Balakumar et al. [9] numerically investigated stability of hypersonic boundary layer over a compression corner using high-order weighted essentially non-oscillatory (WENO) shock-capturing scheme [10]. Zhong et al. conducted a series of numerical simulations related to receptivity and stability of hypersonic flow over: a parabolic leading edge [11–13]; a flat plate [14, 15]; a blunt cone [16] relevant to the Mach = 8 experiments of [17, 18]. These studies were carried out using a high-order shock-fitting scheme.

Though the methods mentioned above allowed for DNS of unsteady processes in compressible flows, new numerical algorithms are desired. Shock-capturing schemes are preferable for practical configurations. However, their robustness is due to relatively high dissipation, which may damp physically unstable disturbances. We attempt to develop a method, which could blend these opposite tendencies. The method is based on the total variation diminishing (TVD) finite volume second-order scheme adapted for non-uniform meshes associated with DNS on bodies of engineering interest. In this paper we demonstrate that the developed method allows for simulation of unstable processes in the boundary layer despite its dissipative features.

As a first step, we carry out DNS of two-dimensional flow fields relevant to stability of the hypersonic boundary layer. Disturbances are generated by local forcing (periodic suction-blowing) on a flat plate at free-stream Mach number 6. For this relatively simple configuration it is feasible to compare numerical solutions with linear stability theory (LST) and validate the method. In addition, physical effects associated with linear and nonlinear dynamics of boundary-layer disturbances are discussed.

2 Numerical method

2.1 Governing equations and boundary conditions

Viscous compressible flows are governed by the Navier–Stokes equations, which result from the conservation laws of mass, momentum and energy. For two-dimensional flows, these equations in an arbitrary curvilinear coordinate system (ξ^*, η^*), where $x^* = x^*(\xi^*, \eta^*)$, $y^* = y^*(\xi^*, \eta^*)$ are Cartesian coordinates, may be written in the conservative form

$$\frac{\partial \mathbf{Q}^*}{\partial t^*} + \frac{\partial \mathbf{E}^*}{\partial \xi^*} + \frac{\partial \mathbf{G}^*}{\partial \eta^*} = 0. \tag{1}$$

Here, asterisks denote dimensional variables, $\mathbf{Q}^*$ is the vector of dependent variables, $\mathbf{E}^*$ and $\mathbf{G}^*$ are the flux vectors in the curvilinear coordinate system. These vectors are expressed in terms of the corresponding vectors $\mathbf{Q}^*_c$, $\mathbf{E}^*_c$, $\mathbf{G}^*_c$ in Cartesian coordinate system as

$$\mathbf{Q}^* = J\mathbf{Q}^*_c, \quad \mathbf{E}^* = J\left(\mathbf{E}^*_c \frac{\partial \xi^*}{\partial x^*} + \mathbf{G}^*_c \frac{\partial \xi^*}{\partial y^*}\right), \quad \mathbf{G}^* = J\left(\mathbf{E}^*_c \frac{\partial \eta^*}{\partial x^*} + \mathbf{G}^*_c \frac{\partial \eta^*}{\partial y^*}\right), \tag{2}$$

where $J = \det \|\partial(x^*, y^*)/\partial(\xi^*, \eta^*)\|$ is the transformation Jacobian. The Cartesian vector components for the two-dimensional Navier–Stokes equations are

$$\mathbf{Q}^*_c = \begin{Vmatrix} \rho^* \\ \rho^* u^* \\ \rho^* v^* \\ e^* \end{Vmatrix}, \quad \mathbf{E}^*_c = \begin{Vmatrix} \rho^* u^* \\ \rho^* u^{*2} + p^* - \tau^*_{xx} \\ \rho^* u^* v^* - \tau^*_{xy} \\ \rho^* u^* H^* - u^* \tau^*_{xx} - v^* \tau^*_{xy} - \lambda^* \frac{\partial T^*}{\partial x^*} \end{Vmatrix},$$

$$\mathbf{G}^*_c = \begin{Vmatrix} \rho^* v^* \\ \rho^* u^* v^* - \tau^*_{xy} \\ \rho^* v^{*2} + p^* - \tau^*_{yy} \\ \rho^* v^* H^* - u^* \tau^*_{xy} - v^* \tau^*_{yy} - \lambda^* \frac{\partial T^*}{\partial y^*} \end{Vmatrix} \tag{3}$$

Here, ρ^* is density; u^*,v^* are Cartesian components of the velocity vector $\mathbf{V}^*$; p^* is pressure; T^* is temperature; $e^* = \rho^*[c^*_v T^* + (u^{*2} + v^{*2})/2]$ is the total energy; $H^* = c^*_p T^* + (u^{*2} + v^{*2})/2$ is the total specific

enthalpy, c_p^*, c_v^* are specific heat capacities at constant pressure and volume, respectively; λ^* is the heat conductivity coefficient; μ^* is the dynamic viscosity coefficient; and τ^* is the stress tensor with the components

$$\tau_{xx}^* = \mu^* \left(-\frac{2}{3} \mathrm{div}\, \mathbf{V}^* + 2\frac{\partial u^*}{\partial x^*} \right), \quad \tau_{xy}^* = \mu^* \left(\frac{\partial u^*}{\partial y^*} + \frac{\partial v^*}{\partial x^*} \right), \quad \tau_{yy}^* = \mu^* \left(-\frac{2}{3} \mathrm{div}\, \mathbf{V}^* + 2\frac{\partial v^*}{\partial y^*} \right). \quad (4)$$

The fluid is a perfect gas with the specific heat ratio $\gamma = 1.4$. The heat conductivity $\lambda^* = \mu^* c_p^*/Pr$ is calculated with the assumption that c_p^* and Prandtl number $Pr = 0.72$ are constant. The viscosity-temperature dependence is approximated by the power law $\mu^*/\mu_\infty^* = (T^*/T_\infty^*)^{0.7}$. Numerical simulations are carried out for hypersonic flow over a flat plate with sharp leading edge. Calculations are conducted at the free-stream Mach number $\mathrm{M}_\infty = 6$ and Reynolds number $Re_\infty = \rho_\infty^* U_\infty^* L^*/\mu_\infty^* = 2 \times 10^6$, where ρ_∞^* is free-stream density, U_∞^* is free-stream velocity, and L^* is the plate length. Hereafter the flow variables are made nondimensional using free-stream parameters, as follows: $(u, v) = (u^*, v^*)/U_\infty^*$, $p = p^*/(\rho_\infty^* U_\infty^{*2})$, $\rho = \rho^*/\rho_\infty^*$, $T = T^*/T_\infty^*$. The nondimensional coordinates and time are $(x, y) = (x^*, y^*)/L^*$, $t = t^* U_\infty^*/L^*$.

The computational domain is a rectangle with its bottom side corresponding to the flat plate surface. The no-slip boundary conditions $(u, v) = 0$ are imposed on the plate surface. The wall temperature corresponds to the adiabatic condition $\partial T_w/\partial n = 0$ for the steady-state solution. Numerical simulations require an additional condition on the wall pressure. This condition is obtained by extrapolation of the near-wall pressure to the plate surface assuming that $\partial p_w/\partial n = 0$. On the outflow boundary, the unknown variables u, v, p, T are extrapolated using the linear approximation. On the inflow and upper boundaries, the conditions correspond to free stream.

The problem is solved in two steps. Firstly, the steady-state solution is calculated to provide the mean flow field. Then, the local suction-blowing is switched on the wall surface at the initial time moment and the unsteady problem is solved. The boundary conditions corresponding to the unsteady problem are formulated in Sect. 3.

2.2 Approximation of differential equations

The problem is solved numerically using a conservative finite-volume method. For calculations of steady-state solution providing the mean flow field, the implicit scheme is more preferable, that helps (in theory) to avoid restrictions on its stability, especially for stiff systems of differential equations. Calculations of unsteady disturbances, in which the time step is very small to provide sufficient accuracy in simulating unstable waves, require less computational time than does the steady-state problem because the steady solution should be obtained with very low numerical residual in the case of small disturbances. Therefore, the implicit numerical scheme is used for both steady and unsteady problems. With this approach Eq. (1) are approximated by the differences equations.

$$\frac{3\mathbf{Q}_{j,k}^{n+1} - 4\mathbf{Q}_{j,k}^{n} + \mathbf{Q}_{j,k}^{n-1}}{\Delta t} + \frac{\mathbf{E}_{j+\frac{1}{2},k}^{n+1} - \mathbf{E}_{j-\frac{1}{2},k}^{n+1}}{h_\xi} + \frac{\mathbf{G}_{j,k+\frac{1}{2}}^{n+1} - \mathbf{G}_{j,k-\frac{1}{2}}^{n+1}}{h_\eta} = 0, \quad (5)$$

where n is the index of time step; j, k are the indices of nodes along ξ, η-coordinates; Δt is the time step; h_ξ, h_η are steps on ξ, η-coordinates, respectively. The second-order temporal discretization (5) is used for unsteady computations, while the first order temporal discretization is used for the steady-state problem.

To approximate the inviscid part of the intercell flux vectors $\mathbf{E}$ and $\mathbf{G}$, the second-order Godunov-type scheme [19] and the approximate [20] method are used for solving the Riemann problem. Then

$$\mathbf{E}_{j+\frac{1}{2}} = \frac{1}{2}[\mathbf{E}(\mathbf{Q}_\mathrm{L}) + \mathbf{E}(\mathbf{Q}_\mathrm{R}) - \mathbf{R}(\mathbf{Q}_\mathrm{LR})\phi(\varphi(\lambda_k))\mathbf{R}(\mathbf{Q}_\mathrm{LR})^{-1}(\mathbf{Q}_\mathrm{R} - \mathbf{Q}_\mathrm{L})], \quad (6)$$

where $\phi(\varphi(\lambda_k))$ is a diagonal matrix with the elements $\varphi(\lambda_k)$; λ_k are eigenvalues of the operator $\mathbf{A} = \partial\mathbf{E}/\partial\mathbf{Q}$. Columns of the matrix $\mathbf{R}(\mathbf{Q}_\mathrm{LR})$ are the right eigenvectors of the operator $\mathbf{A}$. Hereafter the entropy correction function $\varphi(\lambda)$ has the form

$$\varphi(\lambda) = \begin{cases} |\lambda|, & |\lambda| \geq \varepsilon \\ \dfrac{\lambda^2 + \varepsilon^2}{2\varepsilon}, & |\lambda| \leq \varepsilon \end{cases}, \quad (7)$$

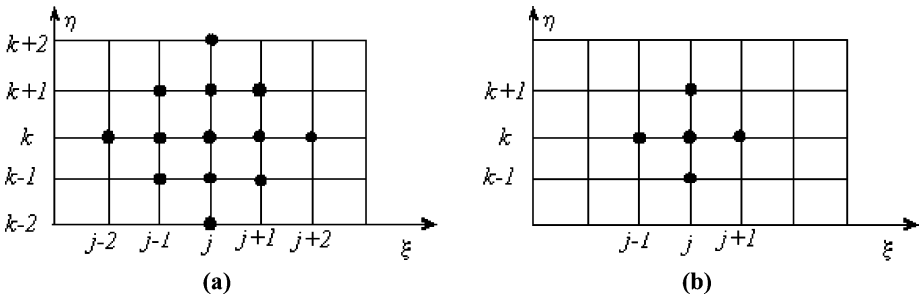

Fig. 1 The stencil of numerical scheme (**a**) and the stencil of Jacobi matrix formation (**b**)

where ε is small parameter (in computations discussed hereafter $\varepsilon = 10^{-3}$). To increase the spatial approximation order to the second order, the principle of minimum derivatives [21] (TVD) is used for interpolation of the dependent variables on the boundary of an elementary cell

$$\mathbf{Q}_{\mathrm{L}} = \mathbf{Q}_j + \frac{1}{2} m(\mathbf{Q}_j - \mathbf{Q}_{j-1}, \mathbf{Q}_{j+1} - \mathbf{Q}_j), \quad \mathbf{Q}_{\mathrm{R}} = \mathbf{Q}_{j+1} - \frac{1}{2} m(\mathbf{Q}_{j+1} - \mathbf{Q}_j, \mathbf{Q}_{j+2} - \mathbf{Q}_{j+1})$$
$$m(a,b) = \begin{cases} \dfrac{2ab}{a+b}, & ab > 0 \\ 0, & ab < 0 \end{cases}, \tag{8}$$

where $m(a, b)$ is the limiter function [22].

Eigenvalues and eigenvectors of the operator $\mathbf{A}$ are calculated using the [20] method of approximated solution of the Riemann problem. To approximate the viscous part of the intercell flux vectors $\mathbf{E}$ and $\mathbf{G}$, a second-order central-difference scheme is used. Direct and mixture derivatives are approximated as

$$\left(\frac{\partial \mathbf{U}}{\partial \xi}\right)_{j+\frac{1}{2},k} = \frac{\mathbf{U}_{j+1,k} - \mathbf{U}_{j,k}}{h_\xi}, \quad \left(\frac{\partial \mathbf{U}}{\partial \eta}\right)_{j+\frac{1}{2},k} = \frac{\mathbf{U}_{j+1,k+1} + \mathbf{U}_{j,k+1} - \mathbf{U}_{j+1,k-1} - \mathbf{U}_{j,k-1}}{4h_\eta}, \tag{9}$$

where $\mathbf{U}$ is the vector of non-conservative problem variables. The difference scheme stencil for the approximation of Navier–Stokes equations consists of thirteen points (Fig. 1a).

2.3 Solution of differences equations

Nonlinear differences equations $\mathbf{F}(\mathbf{X}) = 0$, where $\mathbf{X}$ is the vector of discrete dependent variables for nodal values, are solved using the modified Newton–Raphson [23] method

$$\mathbf{X}^{[k+1]} = \mathbf{X}^{[k]} - \tau_{k+1} \mathbf{D}_{k_0}^{-1} \mathbf{F}\left(\mathbf{X}^{[k]}\right). \tag{10}$$

Here $\mathbf{D}_{k_0} = (\partial \mathbf{F}/\partial \mathbf{X})_{k_0}$ is the Jacobi matrix, k, k_0 are the iteration indices, $k_0 \le k$; the regularization parameter τ_k is determined as

$$\tau_{k+1} = \frac{(\Delta \mathbf{X}^{[k]} - \Delta \mathbf{X}^{[k-1]}, \mathbf{X}^{[k]} - \mathbf{X}^{[k-1]})}{(\Delta \mathbf{X}^{[k]} - \Delta \mathbf{X}^{[k-1]})^2}, \tag{11}$$

where $\Delta \mathbf{X}^{[k]} = \mathbf{D}^{-1} \mathbf{F}(\mathbf{X}^{[k]})$ is the residual vector. As the iteration process converges the regularization parameter tends to 1. Recalculation of the Jacobi matrix is performed only if the decrement of iteration residual is less than 10%.

The Jacobi matrix is formed using the finite differences approach. In general, the operator $\mathbf{D}$ in the approximation of Navier–Stokes equations has the sparse matrix of 13-diagonal block structure. For flows of a perfect gas, its elementary block is a full 4×4 matrix. Herein, the Jacobi matrix is generated using a truncated stencil, which has three nodes in ξ coordinate and three nodes in η coordinate (Fig. 1b). Usage of this truncated stencil essentially decreases the computational time and memory despite some slowing of the convergence process [24]. Then the operator $\mathbf{D}$ has the sparse matrix of 5-diagonal block structure, excluding boundary nodes.

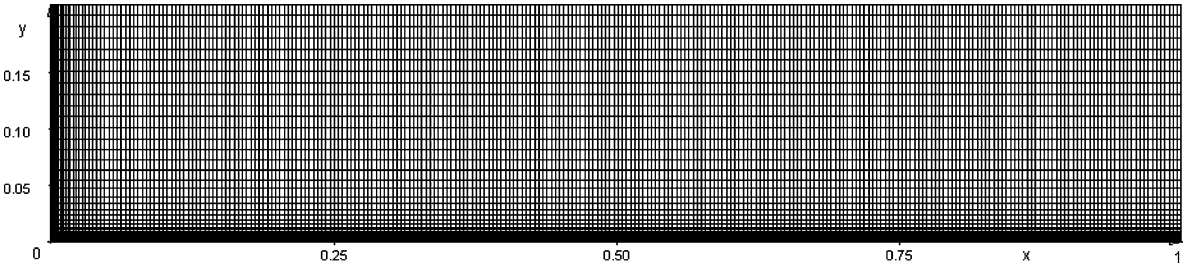

Fig. 2 Grid 1501 × 201, every 5th grid point is shown

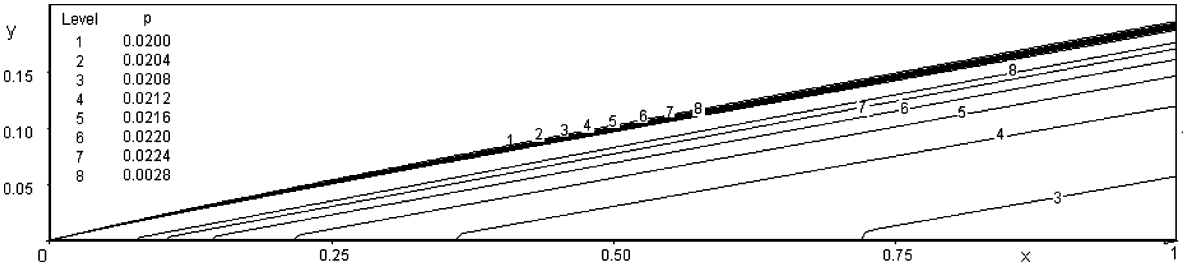

Fig. 3 Pressure contours in the computational domain

In the nonlinear iteration process, a solution of the linear algebraic system is obtained with the help of the iteration general minimum residual method [25] GMRES(k) and *ILU*-decomposition as a preconditioner. Note that the iteration process (compared with the direct method) is sufficiently stable despite simplification of the numerical procedure. This allows for substantial reduction of the CPU time and required memory. The GMRES residual is less than 10^{-7} at each nonlinear iteration.

The computational grid has 1501 × 201 nodes with node clustering [26] near the leading edge and the plate surface (Fig. 2). The boundary layer contains approximately 70 grid nodes in the direction normal to the plate surface at the middle station $x = 0.5$. The residual at each time step achieves 1×10^{-6} for unsteady computations.

3 Results

Numerical simulation is performed for hypersonic flow over a flat plate. Calculations are conducted at the free-stream Mach number $M_\infty = 6$ and the Reynolds number $Re_\infty = \rho^*_\infty U^*_\infty L^*/\mu^*_\infty = 2 \times 10^6$. Figure 3 shows contours of pressure in the computational domain. A shock wave forms in the leading edge vicinity due to viscous-inviscid interaction.

In the boundary-layer region, the numerical solution is compared with the compressible Blasius solution at several downstream locations. As an example, profiles of the longitudinal velocity and temperature are shown in Fig. 4 at the downstream station $x = 0.7$. Small discrepancy between the numerical and Blasius solutions seems to be due to the viscous–inviscid interaction, which was neglected in calculations of the Blasius profiles.

An unsteady disturbance is induced by a local suction-blowing on the plate surface (Fig. 5). This forcing is simulated using the following expression for the mass flow on the plate surface

$$q_w(x,t) = \frac{\rho^*_w v^*_w}{\rho^*_\infty U^*_\infty} = A \sin\left(2\pi \frac{x - x_1}{x_2 - x_1}\right) \sin(\omega t), \quad x_1 \le x \le x_2, \quad t > 0, \tag{12}$$

where A is the forcing amplitude; $x_1 = 0.0358$, $x_2 = 0.0495$ are boundaries of the forcing region; $\omega = \omega^* L^*/U^*_\infty = 260$ is the dimensionless frequency corresponding to the frequency parameter $F = \omega/\mathrm{Re} = 1.3 \times 10^{-4}$. At this frequency the maximum amplitude predicted by LST corresponds to the station $x \approx 0.9$ and relates to the second mode according to the terminology of Mack [27]. Preliminary computations indicated that 1501 grid nodes in the x direction are needed to simulate unstable waves of such frequency with sufficient accuracy.

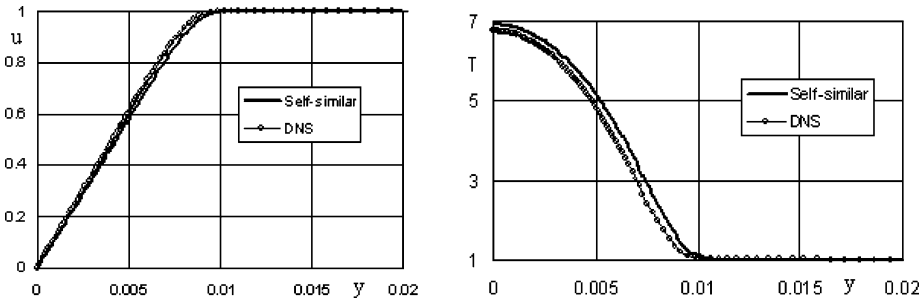

Fig. 4 The longitudinal velocity and temperature profiles resulted from DNS and the self-similar compressible Blasius solution, $M_\infty = 6, Re_\infty = 2 \times 10^6, x = 0.7$

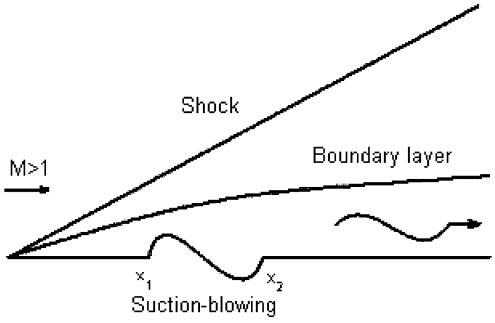

Fig. 5 Sketch of the suction-blowing process

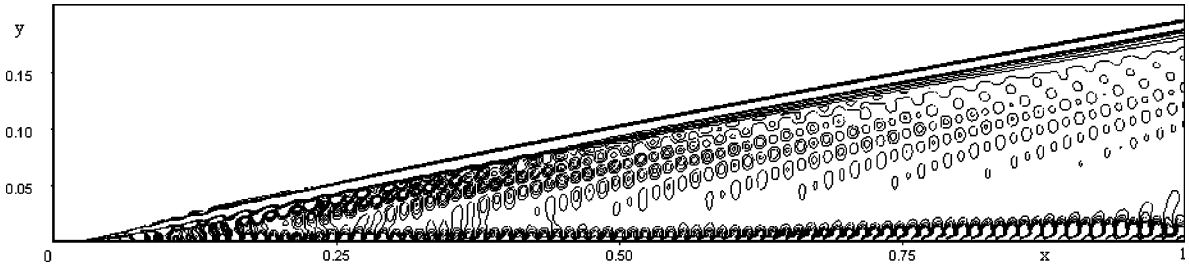

Fig. 6 Disturbance pressure fields induced by the local periodic suction-blowing at $A = 3.6 \times 10^{-2}$ (contour levels are shown from -5×10^{-4} to 5×10^{-4} with step 10^{-4})

Calculations were performed for different forcing amplitudes. The minimal value $A = 6 \times 10^{-4}$ was chosen small in order to compare DNS results with the linear stability theory. For simulation of nonlinear effects, the forcing amplitude is progressively increased as $A = 1 \times 10^{-3}, 1 \times 10^{-2}, 2 \times 10^{-2}, 3 \times 10^{-2}, 3.6 \times 10^{-2}$. In the unsteady problem, the wall temperature equals the adiabatic-wall temperature of the steady solution, $T_w(x, t) = T_{ad}(x)$; i.e., the unsteady temperature disturbance is zero at the plate surface. Note that the disturbance amplitude should be much larger than the numerical error of the steady solution; i.e., the steady flow needs to be calculated with high accuracy. This requirement strongly increases the computational time.

For the unsteady problem, the Navier–Stokes equations are solved until a periodic flow is reached in the entire domain. The difference between unsteady and steady solutions at a fixed moment in time gives an instantaneous disturbance field. A typical example of the pressure disturbance (the forcing amplitude $A = 3.6 \times 10^{-2}$) at a fixed moment in time is shown in Fig. 6. Just downstream of the forcing element at $0.06 < x < 0.2$, the disturbance predominantly consists of acoustic waves trapped by the shock wave. These waves fill up the shock layer. For $x > 0.2$, the acoustic field splits up to the upper region behind the shock wave and the lower region associated with the boundary layer. These regions are separated from each other by a "quiet" zone whose thickness increases downstream. The disturbance field resembles the analytical solutions [28] obtained for acoustic modes in a thin shock layer.

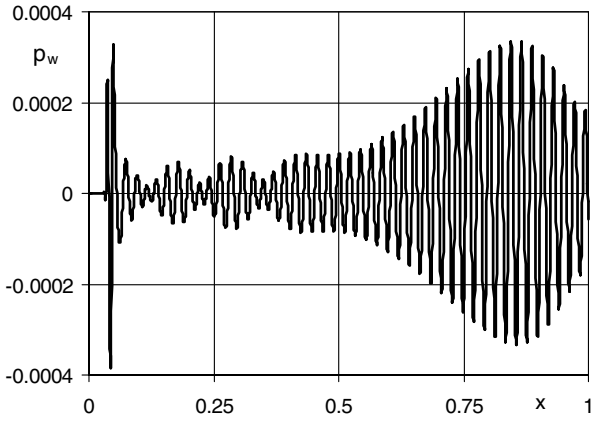

Fig. 7 Pressure disturbance on the plate surface, linear case $A = 6 \times 10^{-4}$

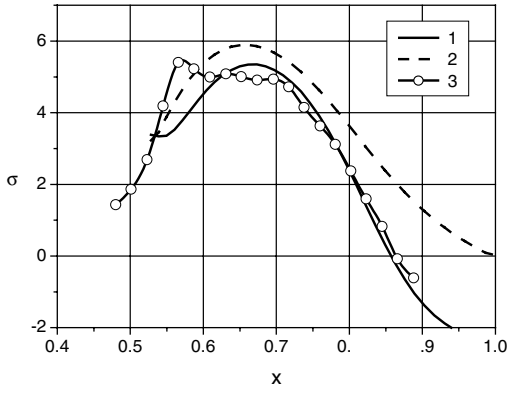

Fig. 8 Growth rates σ of the wall pressure disturbance; (1) nonparallel LST; (2) parallel LST; (3) DNS

At $x \approx 0.5$, the boundary-layer mode starts to grow downstream. The wall pressure disturbance is shown in Fig. 7 at a fixed moment in time. This distribution clearly indicates downstream amplification of the boundary-layer mode for $x > 0.5$. The disturbance growth rate is determined as

$$\sigma = \frac{\mathrm{d}}{\mathrm{d}x}[\ln a(x)] \tag{13}$$

where $a(x)$ is the pressure amplitude on the plate surface. The growth rates resulting from the DNS solution, are compared with those predicted by LST for the second mode [29, 30]. One of these comparisons is shown in Fig. 8. The curve 2 corresponds to the LST data obtained in the local parallel flow approximation; the curve 1 shows the LST data including nonparallel effects; the curve 3 with symbols shows the DNS data. For $x > 0.6$ (where the unstable wave becomes dominant in the boundary layer), the DNS results are in good agreement with the nonparallel LST. This allows us to conclude that the developed code can be used for direct numerical simulation of the boundary-layer instability.

The downstream amplification of boundary-layer disturbances to sufficiently large amplitudes triggers nonlinear interactions. To estimate this effect we performed calculations at various initial amplitudes and plot the maximum wall pressure amplitude $p_{w,\max} = \max[p_w(x)]$ as a function of the forcing amplitude A (see Fig. 9). For $A > 0.015$ the disturbance amplitude deviates from the linear trend and ultimately tends to a constant level. Note that a similar saturation of the second mode was observed on a 7° half angle cone tested in the AEDC Tunnel B at the free-stream Mach number 8 [17].

Comparison of the linear ($A = 6 \times 10^{-4}$) and nonlinear ($A = 3.6 \times 10^{-2}$) cases is shown in Figs. 10 and 11. The difference between these cases is most profound in the region of maximal disturbances in the boundary layer. Detailed snapshots of pressure disturbances for the linear ($A = 6 \times 10^{-4}$) and nonlinear ($A = 3.6 \times 10^{-2}$) cases at a fixed moment in time are presented in Fig. 10. Two-cell structures are formed in the boundary layer. Their longitudinal wavelength approximately equals twice the boundary-layer

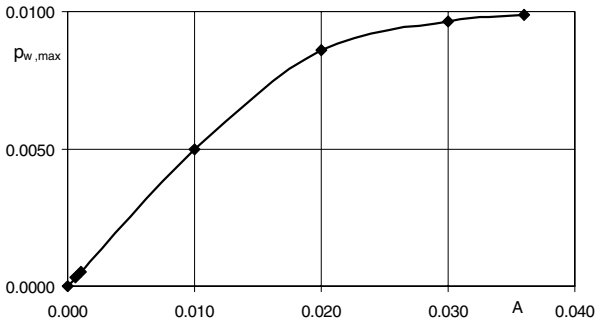

Fig. 9 The wall pressure disturbance maximum, $p_{w,\max} \equiv \max[p_w(x)]$, as a function of the forcing amplitude A

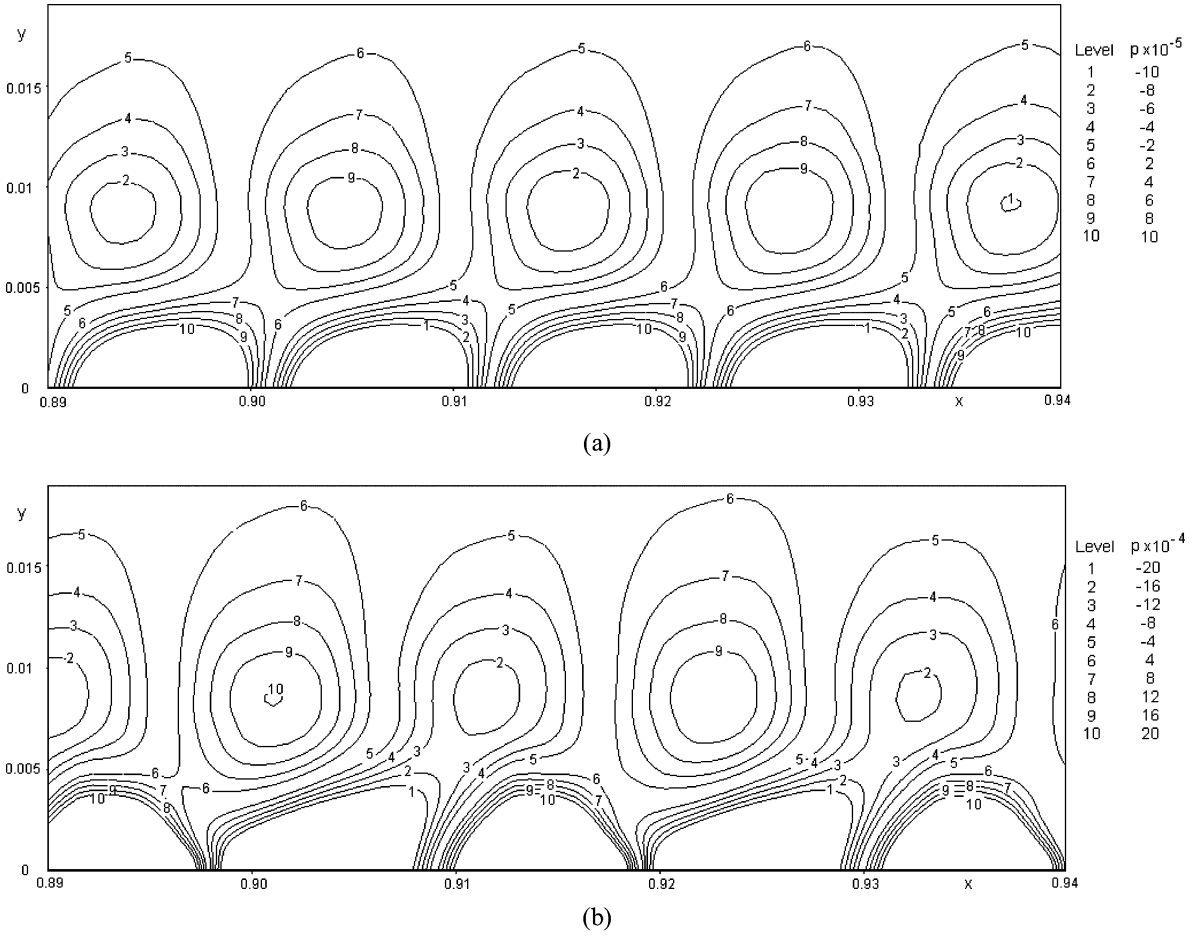

Fig. 10 The pressure disturbance in the boundary layer for the linear (**a**, $A = 6 \times 10^{-4}$) and nonlinear (**b**, $A = 3.6 \times 10^{-2}$) cases

thickness, which is typical for the second mode. Comparing Fig. 10a and b we see that the instantaneous pressure field for a large forcing amplitude ($A = 3.6 \times 10^{-2}$) is different from that observed at a small forcing ($A = 6 \times 10^{-4}$). This difference is most noticeable in the lower cells. Two neighboring cells in x-direction (one of which corresponds to the positive and the other to negative levels of pressure disturbances) have different shapes in the nonlinear case (Fig. 10b) whereas they coincide in the linear case (Fig. 10a).

Distributions of the density disturbance reveal more complicated structures in the boundary layer, especially at large amplitudes. An example of this field is shown in Fig. 11b for the forcing amplitude $A = 3.6 \times 10^{-2}$, the linear case is given for comparison in Fig. 11a. Near the upper boundary-layer edge

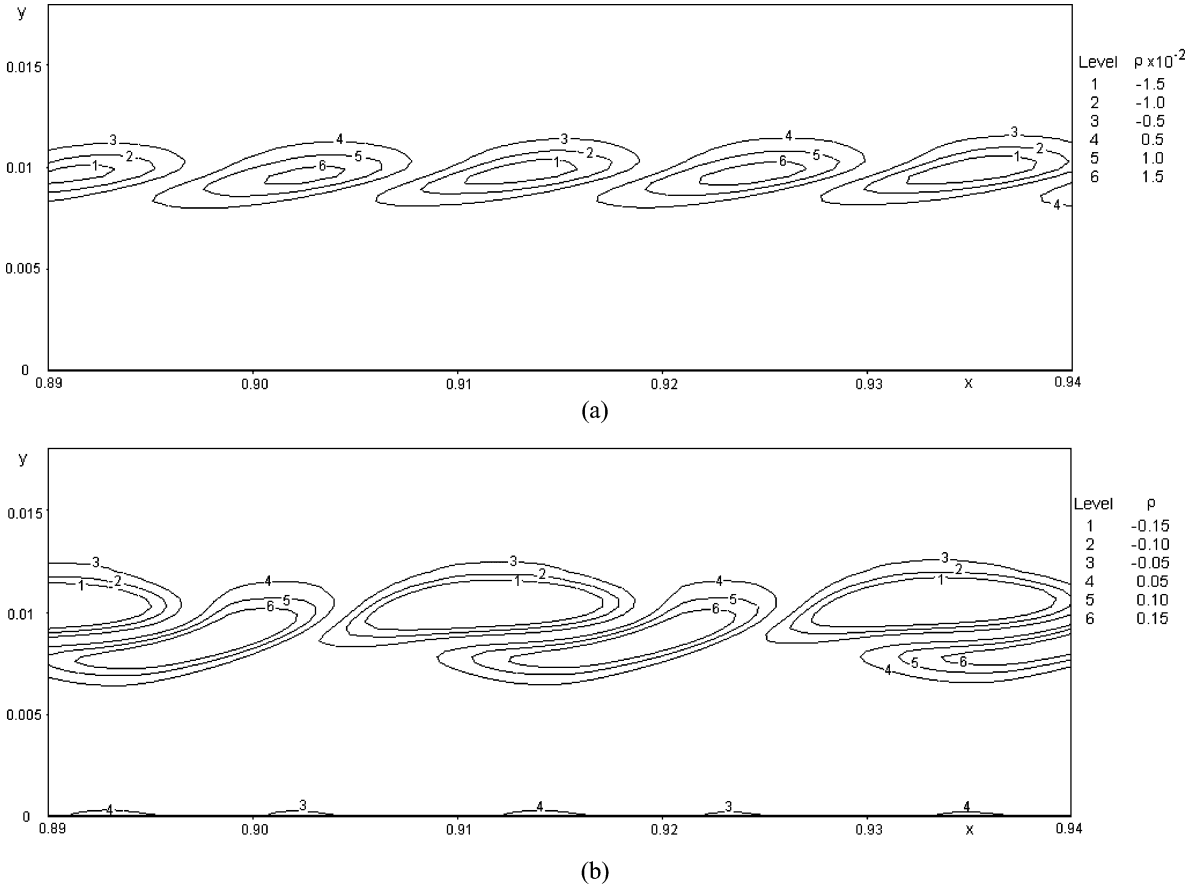

Fig. 11 Density disturbance field for the linear (**a**, $A = 6 \times 10^{-4}$) and nonlinear (**b**, $A = 3.6 \times 10^{-2}$) cases

($y \approx 0.011$), the density disturbance has a structure resembling rope-like waves observed in schlieren images of the experiments [31]. Pruett and Chang [8] performed detailed numerical studies of the rope-like structures and showed that these structures are artifacts of the second-mode disturbances. They generally concurred with Stetson and Kimmel [31] that the original association of "ropes" with secondary instability by Pruett and Zang [32] was in error. This conclusion is consistent with our DNS as well as two-dimensional DNS of [33]. Nevertheless Pruett and Chang [8] noted that the effect of the disturbance obliqueness angle on the appearance of the "ropes" remains unclear, since the equal and opposite oblique second-mode waves may also give rope-like waves in schlieren images.

Figure 11a and b also show that topology of rope-like structures is sensitive to nonlinear effects. For relatively small amplitudes (a) the neighboring cells have almost identical shapes, whereas for large amplitudes (b) these cells are essentially different and their interlacing is more pronounced.

The temperature distribution for the nonlinear case $A = 3.6 \times 10^{-2}$, which includes both the mean flow and disturbance components, is shown in Fig. 12. At the upper boundary-layer edge, there are protuberances, which move slightly faster than structures within the boundary layer. These protuberances slowly roll up similar to vortices in shear layers.

Another interesting feature is observed near the plate wall. Disturbances of large amplitudes induce local separation bubbles, which move downstream with the phase speed of the fundamental harmonic. The shape of these bubbles is visualized by the streamline contours shown in Fig. 13. The maximum upstream velocity U_{sep} in the bubble region is shown in Fig. 14 as a function of the forcing amplitude A. These data indicate the separation bubbles are due to a nonlinear mechanism, which first occurs (in our series of computational cases) at $A = 10^{-2}$. Similar to the behavior of wall-pressure disturbances (Fig. 9), the upstream velocity U_{sep} approaches a plateau as the forcing amplitude A increases.

The total drag coefficient (integrated over plate length), C_x, is shown in Fig. 15 for the case $A = 3.6 \times 10^{-2}$. Its mean value tends to the new level $C_x = 1.66 \times 10^{-3}$, which is slightly higher than $C_x = 1.56 \times 10^{-3}$

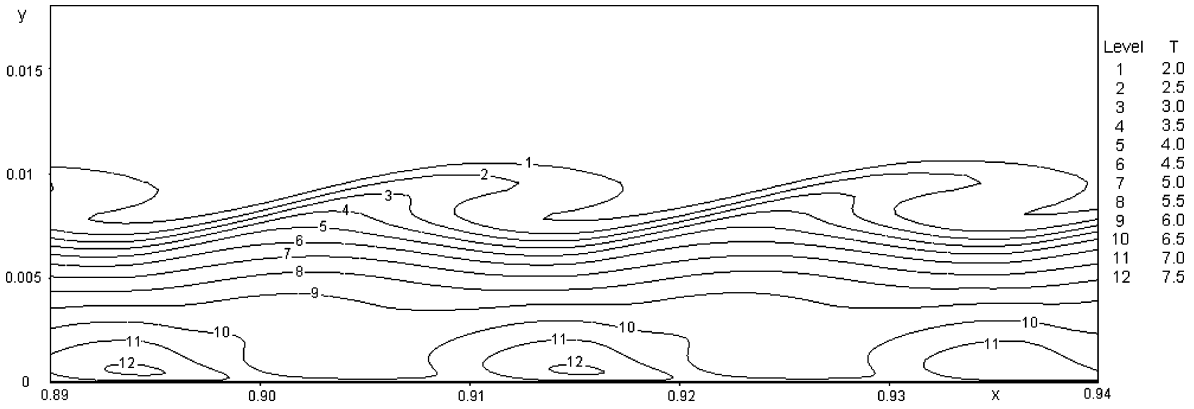

Fig. 12 Temperature field (disturbance plus mean flow) for the nonlinear case $A = 3.6 \times 10^{-2}$

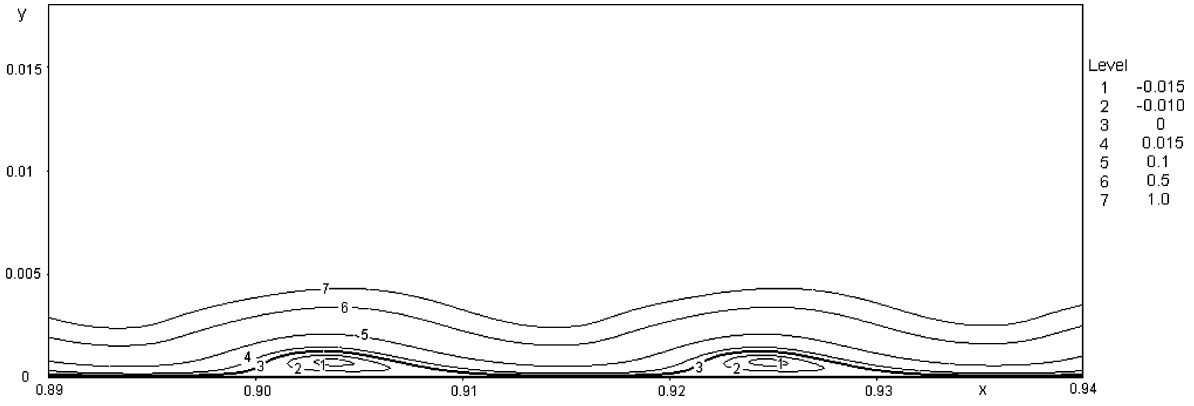

Fig. 13 Streamline contours near the plate surface for the nonlinear case $A = 3.6 \times 10^{-2}$

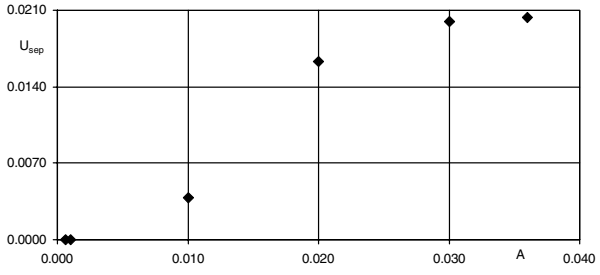

Fig. 14 Maximal upstream velocity U_{sep} in the separation bubbles as a function of the forced amplitude A

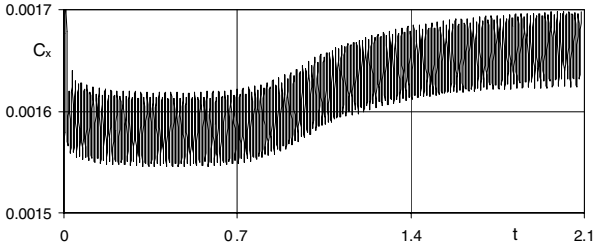

Fig. 15 Time history of the total drag coefficient C_x

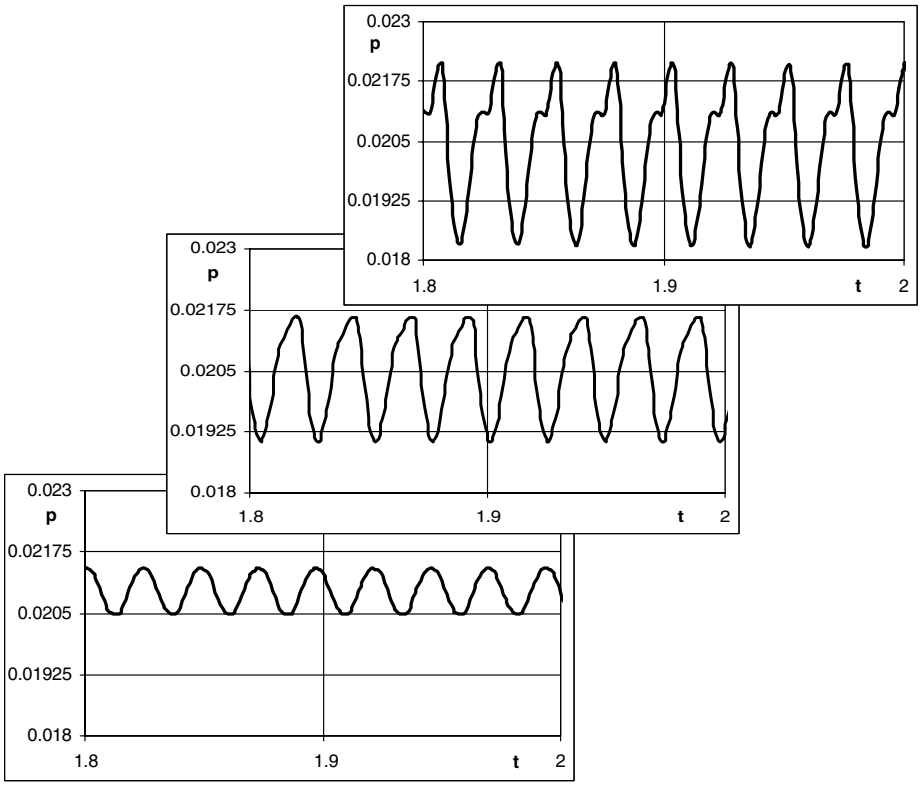

Fig. 16 Pressure oscillations in the boundary layer at $y = 4.2 \times 10^{-3}$; (**a**) $x = 0.52$, (**b**) $x = 0.8$, (**c**) $x = 0.919$

of the undisturbed flow. This is another indication of nonlinearity, i.e., the change of the mean flow by the disturbances.

To investigate nonlinear distortions of disturbances a temporal spectral analysis of pressure fluctuations (induced by suction-blowing with $A = 3.6 \times 10^{-2}$) is performed at the two sets of spatial points (x, y) located in the boundary layer at the stations $x = 0.52,\ 0.8,\ 0.919$: the first set corresponds to the vertical coordinate $y = 4.2 \times 10^{-3}$ lying between two cells of the pressure disturbance field; the second $y = 3.15 \times 10^{-4}$ corresponds to the near-wall region. The first station, $x = 0.52$, is close to the beginning of disturbance growth, the second, $x = 0.8$, corresponds to the unstable region, and the third, $x = 0.919$, is located in the region of the maximal disturbances. For each point (x, y) the temporal spectrum is computed using the fast Fourier transform (FFT) of the pressure oscillogram for the time interval $0 \le t \le 2.1$.

Figure 16 shows the pressure fluctuations at the vertical coordinate $y = 4.2 \times 10^{-3}$. At the first station $x = 0.52$, the signal is purely harmonic. The oscillation peaks become sharper at $x = 0.8$ and, ultimately, new local maximums are formed near the primary peaks at $x = 0.919$. Corresponding spectra, which are normalized to the amplitude of fundamental harmonic of frequency $\omega = 260$, are shown in Fig. 17. Rapid amplification of the second and even third harmonics indicates the presence of nonlinear effects. At the near-wall level $y = 3.15 \times 10^{-4}$, the disturbance spectra (Fig. 18) are dominated by the fundamental harmonic in all three stations.

Note that spectra in Fig. 17 resemble the experimental data of Stetson and Kimmel [31] obtained on a sharp cone at the free-stream Mach number 8. As an example, Fig. 19 shows fluctuation spectra measured with hot-wire anemometer in the boundary layer. The two-dimensional component of second-mode waves (fundamental harmonic) is saturated, whereas the second harmonic experiences rapid growth. There is also indication of the filling of the valleys between the spectral peaks that may be due to low-frequency sideband interactions discussed in the work of Shiplyuk et al. [34]. The DNS spectra in Figs. 17 and 18 do not reveal this effect because the forcing spectrum does not contain low-frequency disturbances typical for wind-tunnel experiments.

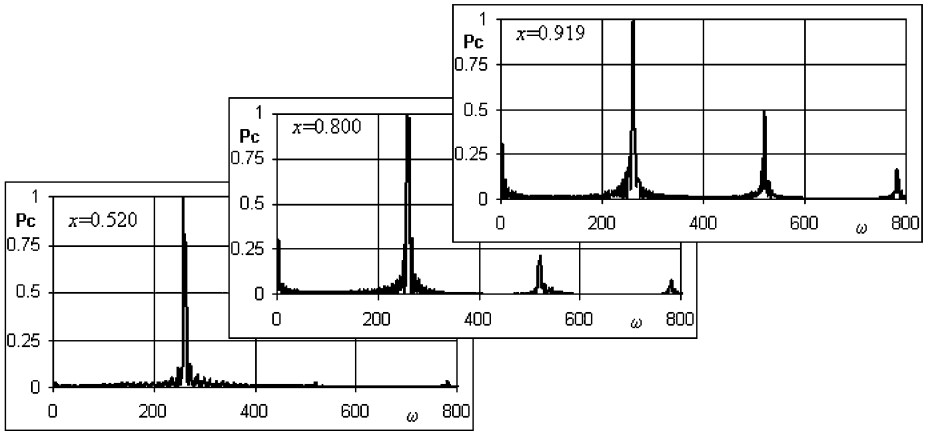

Fig. 17 Normalized spectra of pressure disturbances at $y = 4.2 \times 10^{-3}$

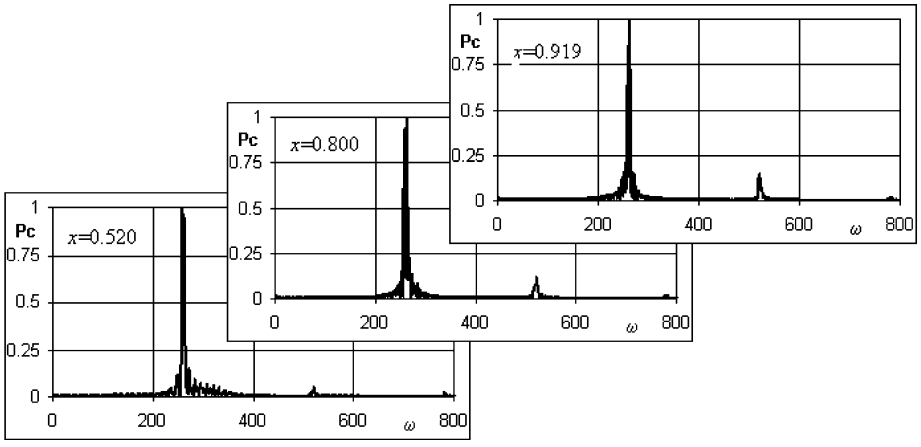

Fig. 18 Normalized spectra of pressure disturbances at $y = 3.15 \times 10^{-4}$

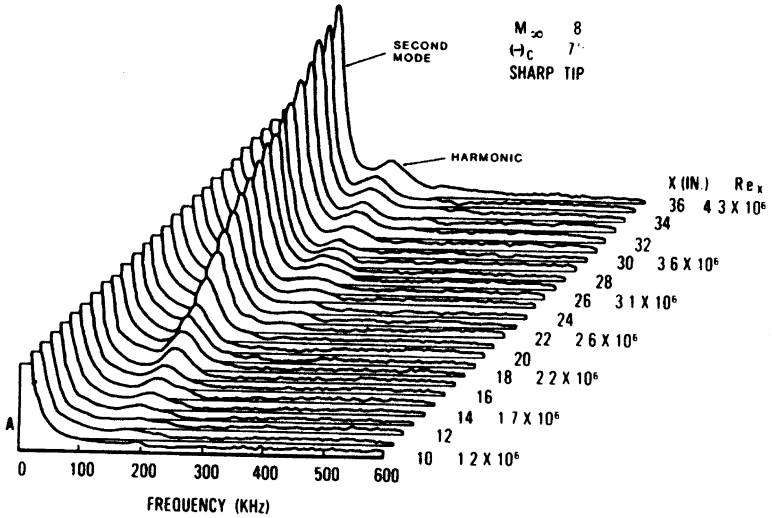

Fig. 19 Fluctuation spectra in the boundary layer on a 7-degree half angle sharp cone at $M_\infty = 8$; scanned from Fig. 4 of Stetson and Kimmel [31]

4 Conclusions

A numerical algorithm and code were developed and applied to DNS of unsteady two-dimensional flow fields relevant to stability of the hypersonic boundary layer. The method is based on the TVD finite volume second-order scheme adapted for non-uniform meshes associated with DNS on bodies of engineering interest.

A numerical simulation of disturbances generated by a periodic suction-blowing on a flat plate was performed at free-stream Mach number 6. It was found that just downstream the forcing element, the disturbance predominantly consists of acoustic waves trapped by the shock wave. Then, the acoustic field splits up to the upper region downstream the shock wave and the lower region associated with the boundary layer. The spatial structure of the boundary-layer disturbance corresponds to the second mode, which amplifies downstream.

For small forcing amplitudes, the second-mode growth rates predicted by DNS agree well with the growth rates from the linear stability theory including nonparallel effects. This shows that the numerical method allows for simulation of unstable processes in the boundary layer despite its dissipative features.

Calculations at large forcing amplitudes indicate the following features of nonlinear dynamics:

- Near the upper boundary-layer edge, the density disturbance has a structure resembling rope-like waves observed in experiments of Stetson and Kimmel [31].
- A nonlinear saturation of the fundamental harmonic is accompanied by rapid growth of the second and third harmonics. This is consistent with the experimental data of Stetson and Kimmel [31] obtained on a sharp cone at the free-stream Mach number 8.
- Near the plate wall, disturbances of large amplitudes induce local separation bubbles, which move downstream with the phase speed of fundamental harmonic.

In future work, the numerical method will be used for DNS of unsteady disturbances in more complicated flows relevant to practical configurations.

Acknowledgements This work is supported by INTAS (Project 00-0007) and the European Office of Aerospace Research and Development (ISTC Project 2393).

References

1. Lin, T.C., Grabowsky, W.R., Yelmgren, K.E.: The search for optimum configurations for re-entry vehicles. J. Spacecraft Rockets **21**(2), 142–149 (1984)
2. Tartabini, P.V., Lepsch, R.A., Korte, J.J., Wurster, K.E.: A multidisciplinary performance analysis of a lifting-body single-stage-to-orbit vehicle. AIAA Paper No. **2000-1045** (2000)
3. Reed, H.L., Kimmel, R., Schneider, S., Arnal, D.: Drag prediction and transition in hypersonic flow. AIAA Paper No. **97-1818** (1997)
4. Malik, M.R.: Boundary-layer transition prediction Toolkit. AIAA Paper No. **97-1904** (1997)
5. Morkovin, M.: Bypass transition to turbulence and research desiderata. Transition in turbulence. NASA CP-2386, 161–199 (1985)
6. Jaffe, N.A., Okamura, T.T., Smith, A.M.O.: Determination of spatial amplification factors and their application to predicting transition. AIAA J. **8**, 301–308 (1970)
7. Chang, C.-L., Malik, M.R.: Compressible stability of growing boundary layers using parabolized stability equations. AIAA Paper No. **91-1636** (1991)
8. Pruett, C.D., Chang, C.-L.: Spatial direct numerical simulation of high-speed boundary layer flows. Part II: Transition on a cone in Mach 8 flow. Theor. Comput. Fluid Dyn. **7**, 397–424 (1995)
9. Balakumar, P., Zhao, H., Atkins, H.: Stability of hypersonic boundary-layer over a compression corner. AIAA Paper No. 2002-2848 (2002)
10. Atkins, H.L.: High-order ENO method for the unsteady compressible Navier-Stokes equations. AIAA Paper No. **91-1557** (1991)
11. Zhong, X.: Direct numerical simulation of hypersonic boundary-layer transition over blunt leading edges. Part I: A new numerical method and validation. AIAA Paper No. **97-0755** (1997)
12. Hu, S.H., Zhong, X.: Linear stability of hypersonic flow over a parabolic leading edge. AIAA Paper No. **97-2015** (1997)
13. Zhong, X.: Receptivity of hypersonic boundary layers to freestream disturbances. AIAA Paper No. **2000-0531** (2000)
14. Ma, Y., Zhong, X.: Direct numerical simulation of instability of nonequilibrium reacting hypersonic boundary layers. AIAA Paper No. **2000-0539** (2000)
15. Ma, Y., Zhong, X.: Direct numerical simulation of receptivity and stability of nonequilibrium reacting hypersonic boundary layers. AIAA Paper No. **2001-0892** (2001)
16. Zhong, X., Ma, Y.: Receptivity and linear stability of stetson's Mach 8 blunt cone stability experiments. AIAA Paper No. **2002-2849** (2002)

17. Stetson, K.F., Thompson, E.R., Donaldson, J.C., Siler, L.G.: Laminar boundary layer stability experiments on a cone at mach 8. Part 2: Blunt cone. AIAA Paper No. **84-0006** (1984)
18. Stetson, K.F., Kimmel, R.L.: On hypersonic boundary layer stability. AIAA Paper No. **92-0737** (1992)
19. Godunov, S.K.: A finite difference method for the computation of discontinuous solutions of the equations of fluid dynamics. Math. Sb. **47**(3), 271–306 (1959)
20. Roe, P.L.: Approximate riemann solvers, parameter vectors, and difference scheme. J. Comput. Phys. **43**, 357–372 (1981)
21. Kolgan, V.P.: The application of minimum derivatives principe to the construction of finite difference schemes to calculate discontinuous solutions of gasdynamics. Uchen. Zap. TsAGI **3**(6), 68–77 (1972)
22. van Leer, B.: Towards the ultimate conservative difference scheme. III. Upstream-centered finite-difference schemes for ideal compressible flow. J. Comput. Phys. **23**(3), 263–275 (1977)
23. Ortega, J.M., Rheinboldt, W.C.: Iterative solution of nonlinear equations in several variables. Academic Press, New York and London (1970)
24. Egorov, I.V., Ivanov, D.V.: Application of Newton's method in simulation of unsteady separated flows. Comput. Math. Math. Phys. **38**(3), 488–492 (1998)
25. Babaev, I.Yu., Bashkin, V.A., Egorov, I.V.: Numerical solution of Navier–Stokes equations by using iteration variation-type methods. J. Comput. Math. Math. Phys. **34**(11), 1693–1703 (1994)
26. Bashkin, V.A., Egorov, I.V., Ivanov, D.V.: The application of the newton method to simulate inner supersonic separated flows. Prikl. Mekh. i Tekh. Fiz. **1**, 30–42 (1997)
27. Mack, L.M.: Linear stability theory and the problem of supersonic boundary layer transition. AIAA J. **13**, 278–289 (1975)
28. Guschin, V.R., Fedorov, A.V.: Short-wave instability in a perfect-gas shock layer. Fluid Dyn. **24**(1), 7–10 (1989)
29. Fedorov, A.V., Khokhlov, A.P.: Prehistory of instability in a hypersonic boundary layer. Theoret. Comput. Fluid Dyn. **14**(6), 359–375 (2001)
30. Fedorov, A.V., Khokhlov, A.P.: Receptivity of hypersonic boundary layer to wall disturbances. Theoret. Comput. Fluid Dyn. **15**(4), 231–254 (2002)
31. Stetson, K.F., Kimmel, R.L.: On the breakdown of a hypersonic laminar boundary layer. AIAA Paper No. **93-0896** (1993)
32. Pruett, C.D., Zang, T.A.: Direct numerical simulation of laminar breakdown in high-speed, axisymmetric boundary layers. AIAA Paper No. **92-0742** (1992)
33. Ma, Y., Zhong, X.: Receptivity of a supersonic boundary layer over a flat plate. Part 2: Receptivity to free-stream sound. J. Fluid. Mech. **488**, 79–121 (2003).
34. Shiplyuk, A.N., Bountin, D.A., Maslov, A.A., Chokani, N.D.: Nonlinear interactions of second mode instability with natural and artificial disturbances. AIAA Paper No. **2003-0787** (2003)